Mapping Star Formation Histories in Nearby Galaxies to Source Lyman Continuum Photon Escape

Katherine Kudla, Crystal L. Martin, Zixuan Peng, and Yuan Li
Department of Physics, Broida Hall, University of California at Santa Barbara, Santa Barbara, CA 93106, USA
(Dated: September 26, 2023)

Our current understanding of the Epoch of Reionization (EoR) elicits many uncertainties. It is unknown how Lyman continuum photons, responsible for ionizing neutral hydrogen during this epoch, reached the intergalactic medium. One theory of their escape pertains to galactic winds. The intense outflows of gas and particles from supernovae and other large-scale astronomical phenomena create "holes" in the interstellar clouds, thereby facilitating Lyman continuum photon escape. To explore this theory, we need to define the stellar complexes within galaxies from the EoR; through mapping their star formation histories, we can better understand the interactions between stellar populations and use this to source Lyman continuum photon escape. Because galaxies from the EoR are billions of light-years away, we study 6 nearby Extreme-Emission-Line-Galaxies (EELGs), considered local analogs of those from the EoR. We use integral field spectroscopy to extract and analyze the emission and absorption spectra for each stellar complex. Through fitting their Balmer lines, we quantify their emission- and absorption-line equivalent widths. Greater emission-line equivalent widths correspond to younger populations, while greater absorption-line equivalent widths correspond to older populations. Upon approximating the stellar population ages based on these equivalent widths, we search for spatial offsets between younger stars, responsible for producing Lyman continuum photons, and older stars, responsible for creating "holes" in interstellar clouds from their core-collapses. We find that, while there are trends in star formation histories amongst pairs of galaxies, there are few consistencies that apply to the entire sample.

Keywords: Galactic outflows, Reionization Epoch, Lyman continuum photon escape, Balmer lines, Stellar Population Synthesis

I. INTRODUCTION

The Epoch of Reionization (EoR), or final transition phase of the universe, occurred between 150 million years and 1 billion years after the Big Bang. This was when photons escaped galaxies and ionized the neutral hydrogen in the intergalactic medium (IGM) and circumgalactic medium (CGM) [1]. While it occurred billions of years ago, this ionization is crucial to the formation and evolution of galaxies in our local universe.

It is a mystery how these Lyman continuum photons penetrate through the interstellar clouds that inhabit these galaxies. One theory pertains to different stellar populations and their relationships with one another. O-type stars are young (millions of years old) and massive ($10-20$ $M_\odot$). They radiate energy in the form of Lyman continuum photons, photons with energies greater than or equal to the minimum energy needed to ionize neutral hydrogen: 13.6eV. While these photons and their escapes are needed for the EoR, they are unable to reach the IGM or CGM, should there exist no paths for such escape. If this is the case, the interstellar clouds absorb these photons and they are unable to reach the neutral hydrogen in the surrounding media. A-type stars are much older than O-type stars (10-100 million years old). They eventually become core-collapse supernovae and produce galactic winds, intense outflows of gas and particles. Whether these outflows reach the IGM or merely redistribute themselves throughout the interstellar medium (ISM) depends on (1) the mass of the galaxy, directly influencing its gravitational potential well and (2) the energy of the event creating the galactic wind. While galactic winds transport gases and particles themselves, they also create "holes" in the interstellar clouds, thereby facilitating future photon escape.

The uncertainty surrounding the Reionization Epoch, particularly Lyman continuum photon escape, can potentially be resolved with the union of these two stellar classifications. Should a galaxy contain O-type stars, producing Lyman continuum photons, as well as A-type stars, producing galactic winds and thus "holes" in the interstellar clouds, the ambiguity behind the escape of Lyman continuum photons during the EoR may be resolved.

To investigate this theory, we map and study the star formation histories in 6 nearby Extreme-Emission-Line galaxies (EELGs) observed by the CLASSY Team [2]. Despite their low redshifts (z=0.001-0.01), they closely resemble galaxies from the EoR. Their low masses ($\log(M)=6-8$), low metallicities ($\log(Z)=0.01-0.1$), irregular morphologies, and high specific star formation rates ($\log(sSFR) = -8 - -7$) are select characteristics that name them local analogs.

From each galaxy's Hubble Space Telescope (HST), Dark Energy Spectroscopic Instrument (DESI), or Sloan Digital Sky Survey (SDSS) images, we define their different stellar complexes. Upon extracting spectra from the Keck Cosmic Web Imager (KCWI) for each of these regions, we fit the emission and absorption components of their Balmer lines. Then, we calculate and compare the Balmer emission- and absorption-line equivalent widths to those generated by state-of-the-art stellar population

synthesis tool, BEAGLE [3]. This comparison, via an equivalent width grid, provides an age approximation for each stellar complex. In addition to mapping the distribution of stellar complex ages for each galaxy, we spatially resolve the galaxy images to further assess the above proposed theory of Lyman continuum photon escape.

II. METHODS

A. Identifying Stellar Complexes

We utilized `Photutils` to group clusters of stars, called stellar complexes, within the galaxies that made up our sample. To begin, we located and extracted HST, DESI, or SDSS images, in the same band, for each galaxy in our sample. To account for background noise, we extracted an uncontaminated region of the galaxy's image and used its median noise value to derive the threshold parameter. We multiplied this value by a factor of 8 for these galaxies, all background-subtracted, to obtain the threshold values. Then, we constructed a segmentation image for each galaxy through quantifying each pixel in the galaxy image. Because certain brightnesses/intensities share such quantities, the galaxy images were resolved into different clusters of stars. Upon establishing preliminary stellar complexes, we better defined these regions through deblending the segmentation image; this divided the stellar complexes into smaller, more precise clusters through taking into account their overlap. This was done through defining three parameters: number of connecting pixels (npixels), number of levels (nlevels), and contrast (Table 1). We defined the number of connecting pixels through measuring the number of pixels per arcsecond in each image and calculating npixels=$\pi\times$(pixels/arcsec)^2. 1" is the point spread function full width at half maximum (PSF FWHM) size of the KCWI data cubes (see Section II.B.), and so it is not physical to extract spectra for regions any smaller than this. For galaxies with identical segmentation and deblending images, we adjust the number of connecting pixels by decreasing it by a factor of $\pi : npixels = (pixels/arcsec)^2$. We defined 512 multi-thresholding levels. Lastly, we used 1% contrast to deblend each galaxy segmentation. Depending on the resolution, size, and morphology of each galaxy, unique stellar complexes were identified (Figure 1).

Ultimately, with a precise identification of the different stellar complexes in each sample galaxy, we constructed their region apertures through calculating the Petrosian radius using `Petrofit`. This method utilizes the photometry-derived curve of growth to identify the radii enclosing different fractions of the total flux. Ultimately, the Petrosian radius is defined below, such that R_1 and R_2 represent the radii one before and one after the Petrosian radius:

$$R_{petrosian} = 0.2 \times \frac{R_1 + R_2}{2} \qquad (1)$$

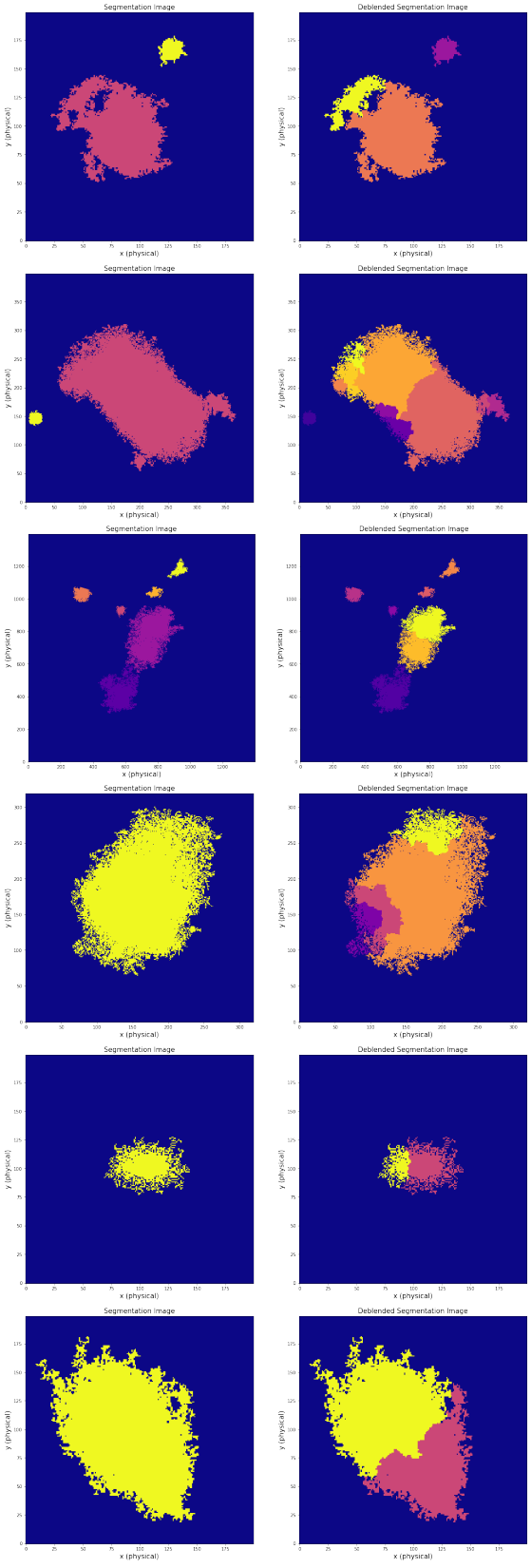

FIG. 1. *Left:* Segmentation images of J0248, J0823, J0944, J1016, J1238, and J1418 (top to bottom).
Right: Deblended segmentation images of same galaxies beside their segmentation images.

Galaxy ID	RA:DEC	Redshift	Image Origin	Filter	Threshold	npixels	nlevels	Contrast
J0248	02:48:15.82-08:17:23.8	0.004562	HST	F814W	0.0432818010	400	512	0.01
J0823	08:23:34.84+03:13:15.6	0.009777	HST	F110W	1.4175570488	50	512	0.01
J0944	09:44:01.87-00:38:32.2	0.00478	HST	F814W	0.0065636460	2100	512	0.01
J1016	10:16:24.48+37:54:46.0	0.00388	HST	F814W	0.0567662762	156	512	0.01
J1238	12:38:06.88+10:09:56.0	0.00855	SDSS	I−BAND	0.0105636963	20	512	0.01
J1418	14:18:51.11+21:02:39.8	0.003795	HST	F275W1	0.0027794047	625	512	0.01

TABLE I. For each galaxy in our sample, its reference ID (according to this paper), WCS coordinates, image source, image filter, and segmentation/deblending parameters are provided.

Derived from the Petrosian radius, additional radii were calculated at 20%, 50%, 80%, and 100% the total flux radius (Figure 2). Galaxy coverage was assessed for each plotted radius. At varying fractions of enclosed flux, depending on the galaxy, we record the radius that maximized stellar complex coverage across the galaxy, while avoiding redundancies from overlapping regions. Using each stellar complex's spatial coordinates and elliptical properties (Table 2), we defined these apertures on each galaxy image and extracted a region file, at the specified radius, from DS9.

The Petrosian-derived elliptical apertures are convenient and easily quantified. This was the first way we analyzed each identified stellar complex separate from the rest of the galaxy. To further maximize galaxy coverage, while minimizing region overlaps, we also extracted free-form polygon apertures, defined by the perimeters of the deblended segmentation images of each galaxy. Through directly extracting region files from our deblended segmentation images, we have access to two types of apertures defining the stellar complexes in our galaxy sample. Ultimately, we map the star formation histories of the same stellar complexes within each galaxy using (1) elliptical apertures, and (2) free-form polygon apertures.

S.C.	Enc. Flux	Center	b/a	θ
J0248-A	80%	(362,640)	0.875	68.620
J0248-B	80%	(312,556)	0.902	44.653
J0248-C	80%	(283,600)	0.356	48.785
J0823-A	80%	x	x	x
J0823-B	80%	x	x	x
J0823-C	80%	x	x	x
J0823-D	80%	x	x	x
J0823-E	80%	x	x	x
J0944-A	100%	(7614,9266)	0.819	48.748
J0944-B	100%	(7419,9120)	0.961	20.323
J0944-C	100%	(7429,8936)	0.824	5.809
J0944-D	100%	(7358,8751)	0.552	-46.186
J0944-E	100%	(7220,8550)	0.650	76.093
J1016-A	50%	(205,1781)	0.579	64.605
J1016-B	50%	(226,1784)	0.604	-61.388
J1016-C	50%	(237,1827)	0.812	72.606
J1016-D	50%	(276,1893)	0.713	-3.693
J1238-A	50%	(1863,801)	0.877	1.056
J1238-B	50%	(1843,798)	0.740	78.078
J1418-A	80%	(6100,3589)	0.754	81.190
J1418-B	80%	(6141,3520)	0.970	63.881

TABLE II. In addition to defining the stellar complexes identified in each galaxy (corresponding to their labels in Figure 2), we define the elliptical apertures at a given Petrosian-derived radius.

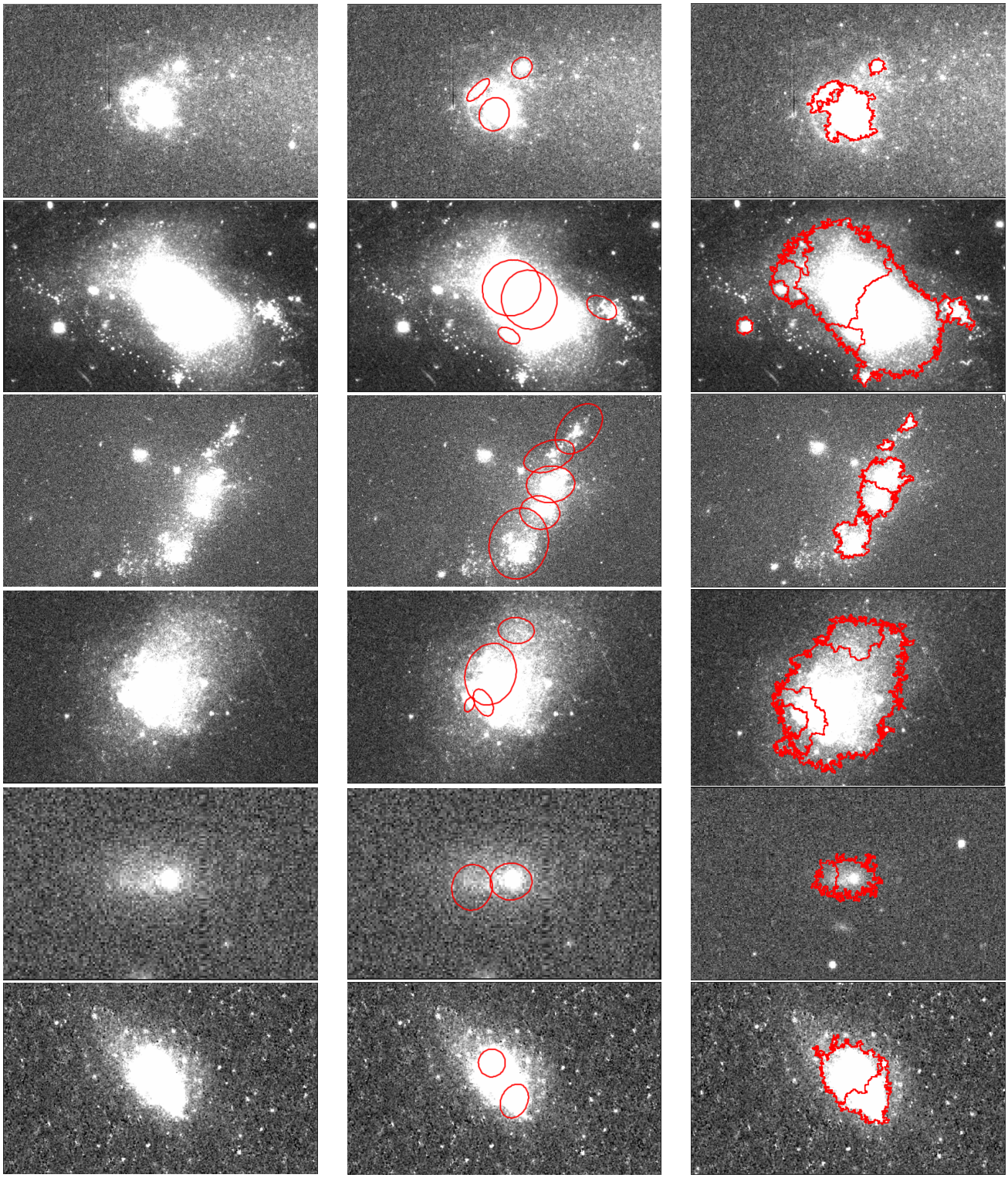

FIG. 2. *Left:* Each galaxy in our sample (J0248, J0823, J0944, J1016, J1238, J1418 top to bottom)
Middle: Each galaxy marked with elliptical apertures derived from their Petrosian radii.
Right: Each galaxy marked with free-form-polygon apertures in the shape of their deblended regions.

B. Extracting KCWI 1D Spectra

For each stellar complex we identified in Section II. A., we extracted their emission and absorption spectra from the Keck Cosmic Web Imager (KCWI). The KCWI is an instrument that uses integral field spectroscopy to collect spectral data for every observed spaxal defining a source. These spectra range from wavelengths of 3500 to 5600 Å [4]. To extract flux and variance spectra for each stellar complex, we used `Pyregion` on the elliptical and free-form-polygon apertures defining each. Upon extracting the flux spectrum and variance spectrum for each stellar complex, we analyzed the Balmer lines present in their spectra.

1. *Using Balmer Lines as an Age Indicator*

The Balmer series defines the spectral line emissions and absorptions present in hydrogen. When hydrogen excites from the second energy state, Balmer line absorption troughs form. When hydrogen deexcites to the second energy state, Balmer line emission peaks form. When we analyze Balmer lines, the emission peaks are representative of younger stellar populations. These peaks are from the nebulae surrounding stars. As stars radiate significant energy, enough to excite the surrounding nebulae, these emission lines form from their eventual deexcitation. Thus, Balmer line emissions are indicative of younger, more massive O-type stars. The absorption troughs, while they are present for all stellar populations, are representative of older stellar populations. The troughs are from the stars themselves, and so they will be present for all stellar populations, whether they are observable or not. These troughs are only observable when the emission peaks are small enough, or non-existent. Thus, Balmer line absorptions, which are only seen for stars that are radiating significantly less energy than O-type stars, are indicative of older A-type stars. Ultimately, Balmer line emissions and absorptions are particularly relevant when mapping stellar population ages, and hence star formation histories, due to their sensitivity to stellar age.

2. *Fitting Balmer Lines*

We observed and fit the Balmer lines of each stellar complex to Gaussian, Lorentzian, or "Gaussian plus Lorentzian" profiles, depending on their emission and absorption strengths. To do this, we utilized the line fitting program, `LMFIT` [5]. For the emission and/or absorption lines selected, this program iterates through 1000 unique parameters, conducting an F-Test in search of a "best fit." This is defined, statistically, by the lowest possible χ^2 value:

$$\chi^2 = \sum (\frac{model - data}{error})^2 \tag{2}$$

S.C.	Hγ EW(EM)	Hγ EW(AB)	Hδ EW(EM)	Hδ EW(AB)
J0248-A	74.806	—	35.979	—
J0248-B	125.823	—	59.145	—
J0248-C	58.437	—	28.582	—
J0823-A	0.641	6.894	0.040	5.775
J0823-B	0.732	7.684	0.284	7.043
J0823-C	33.007	4.131	15.502	4.653
J0823-D	1.827	6.813	0.668	4.875
J0823-E	0.949	6.812	0.436	7.652
J0944-A	82.633	—	37.023	—
J0944-B	41.029	—	18.340	2.748
J0944-C	87.483	—	39.143	1.096
J0944-D	41.569	—	18.506	3.628
J0944-E	21.242	3.820	9.118	3.803
J1016-A	75.374	—	32.897	—
J1016-B	44.361	—	19.518	3.321
J1016-C	42.837	6.456	18.665	6.462
J1016-D	14.292	—	9.753	—
J1238-A	34.524	—	16.651	4.013
J1238-B	1.294	4.721	0.596	7.001
J1418-A	68.604	—	28.828	—
J1418-B	53.979	—	22.271	—

TABLE III. For each stellar complex, we fit the Hγ and Hδ Balmer lines and quantify their emission and absorption strengths through integrating flux of the emission and/or absorption against the flux continuum.

C. Quantifying Emission and Absorption Components of Balmer Lines

Once we fit their Balmer lines, we calculated their emission and absorption equivalent widths (EW), defined by the following integrals:

$$EW_{emission} = \int \frac{F_\lambda}{F_{continuum}} - 1 \, d\lambda \tag{3}$$

$$EW_{absorption} = \int 1 - \frac{F_\lambda}{F_{continuum}} \, d\lambda \tag{4}$$

The corresponding EWs of Hγ and Hδ emission and absorption for each stellar complex are listed in Table 3. For many of the younger stellar complexes, as well as those with particularly broad absorption troughs, the fitting program was unable to register absorptions. For these stellar complexes, there was a defined EW(EM), but no EW(AB). This does not mean there is no absorption; instead, however, it means there are infinite fits the program can iterate through. Rather than listing one of these iterations, we replace the EW(AB) with "—".

D. Quantifying Stellar Population Ages with BEAGLE

With quantified equivalent widths for each stellar complex in each of our sample galaxies, we compared the emission and absorption strengths to approximate the relative ages of these stellar complexes; however, this approximation is merely qualitative. Using state-of-the-art stellar population synthesis (SPS) model BEAGLE (BayEsian Analysis of GaLaxy sEds), we quantify these age approximations. Through setting parameters in stellar mass, stellar and gas-phase metallicity, specific star formation rate, timescale of the recent burst we are simulating, ionization parameter, dust-to-metal mass ratio, and attentuation, we generated mock spectra for a galaxy modelled to resemble those that made up our sample (Table 4). Three sets of mock spectra were generated, as we assumed three potential star formation history models: Pure Single Stellar Population (SSP), Constant Star Formation, and Composite (SSP and Constant). All three sets contain mock spectra with quantified emissions and absorptions at different time stamps. The earliest spectrum is generated for the mock galaxy at 1,000,000 years, the latest is at 1,000,000,000 years, and 60 additional spectra are created at times spaced logarithmically between these two extremes.

Once these mock spectra were generated, we calculated their Balmer line equivalent widths, thus quantifying their emissions and absorptions, as explained in Section II.C. Using these calculated values, we construct EW grids, one for Hγ and another for Hδ, with the EW of emission (EW(EM)) along the x-axis and EW of absorption (EW(AB)) along the y-axis. Color-coded with respect to age, this grid depicts how emission and absorption strengths vary with age. Upon over-plotting the EW(EM) and EW(AB) calculated from each stellar complex's extracted 1D spectrum, we approximate their ages depending on their positions on the grid, specifically relative to the mock spectra. Knowing the age distribution of stellar complexes in a galaxy is valuable in learning more about their star formation histories. In addition to mapping the star formation histories of each of the 6 sample galaxies, we spatially resolve their images, such that we can see these star formation histories as well.

III. STAR FORMATION HISTORIES: MAPPING AND ANALYSIS

A. Results

For each stellar complex, its error in EW(EM) is derived from the median value of the LMFIT-calculated error array, derived from the χ^2 of our Balmer line fits. The error in EW(AB) varies depending on whether or not it is defined numerically in Table 3. For the stellar complexes with defined EW(AB), the error is derived just as EW(EM) was. For the stellar complexes without defined EW(AB), however, the EW(AB) of the mock spectrum point closest in EW(EM) is set as the upper limit (depicted by a downward arrow in place of error bars in Figure 3).

In galaxy J0248, the youngest stellar complex is approximately 3,548,134 years old, and the oldest stellar complex is approximately 11,220,185 years old. Two of the three stellar complexes fall in the age range of O-type stars, while the third falls in the range of B-type stars. The star formation history, spatially, shows a southeastern propagation, with minimal resolution in the two eastern stellar complexes.

In galaxy J0823, the youngest stellar complex is approximately 39,810,717 years old, and the oldest stellar complex is approximately 251,188,643 years old. Four of the five stellar complexes fall in the age range of A-type stars, while the fifth falls in the age range of B-type stars. The star formation history, spatially, shows an inward propagation, with the B-type stellar population surrounded by A-type stellar populations.

In galaxy J0944, the youngest stellar complex is approximately 5,623,413 years old, and the oldest stellar complex is approximately 35,481,339 years old. Three of the five stellar complexes fall in the age range of B-type stars, while the remaining two fall in the range of O-type stars. The star formation history, spatially, shows two inward propagations, as the center-most and two outermost stellar complexes are significantly older than the remaining two.

In galaxy J1016, the youngest stellar complex is approximately 8,912,509 years old, and the oldest stellar complex is approximately 112,201,845 years old. One of the four stellar complexes falls in the age range of A-type stars, two of the four stellar complexes fall in the age range of B-type stars, and the last stellar complex falls in the range of O-type stars. The star formation history, spatially, shows a northwestern propagation, with the starburst and post-starburst regions being separated by significantly larger B-type stellar complexes.

In galaxy J1238, the youngest stellar complex is approximately 22,387,211 years old, and the oldest stellar complex is approximately 50,118,723 years old. Both stellar complexes fall in the age range of B-type stars; however, the older of the two crosses into the age range of A-type stars, upon considering its error. The star formation history, spatially, shows consistently B-type stellar populations. Despite one stellar complex being more than twice as old as the other, both are too old to radiate Lyman continuum photons, but neither are too young to become core-collapse supernovae.

In galaxy J1418, the youngest stellar complex is approximately 5,011,872 years old, and the oldest stellar complex is approximately 10,000,000 years old. One stellar complex falls in the age range of O-type stars, while the other falls in the age range of B-type stars. The star formation history, spatially, shows a northeastern propagation, with a relatively smaller age distribution than that present in the other galaxies.

Across all 6 galaxies we found that:

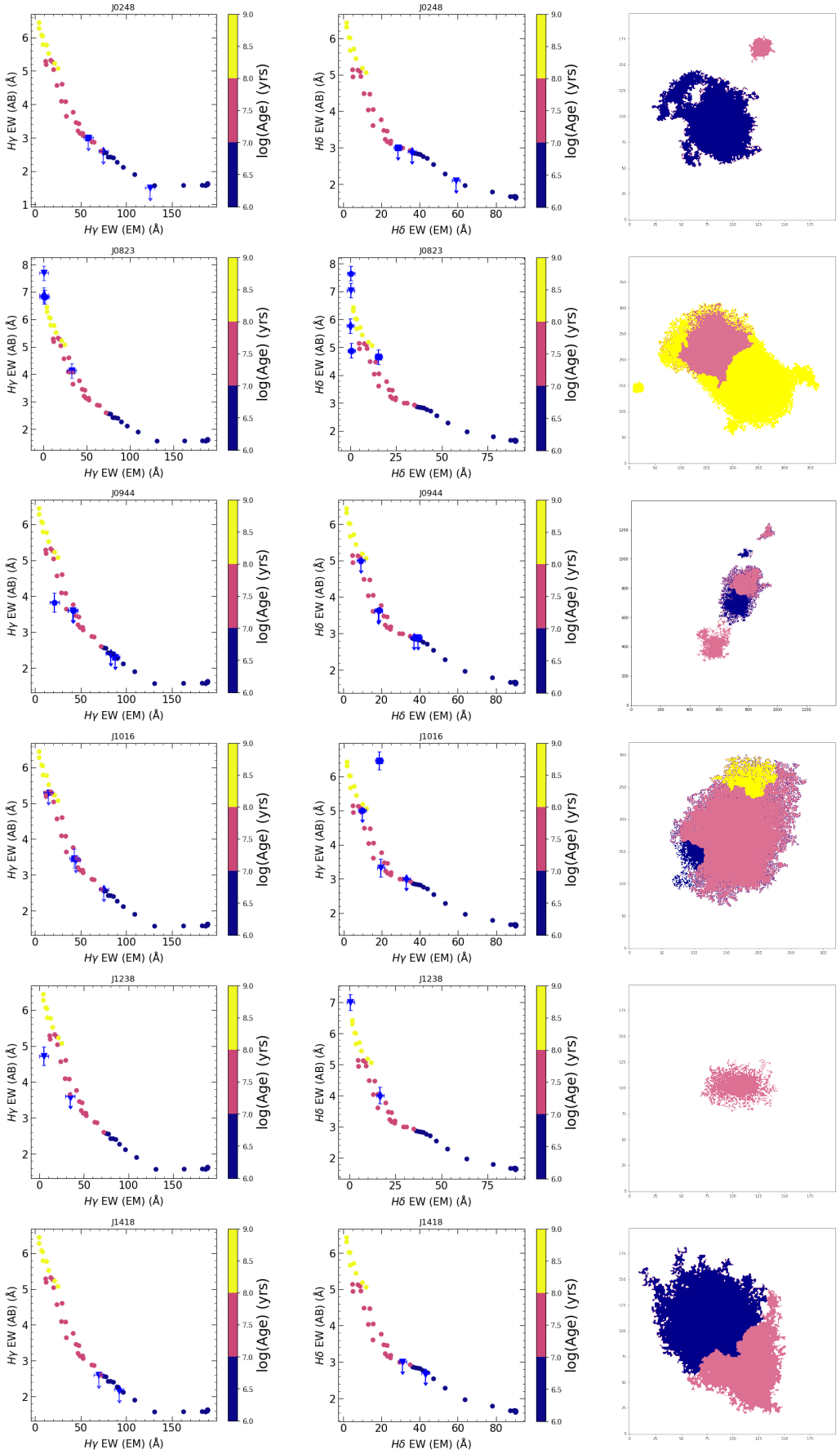

FIG. 3. Each row contains the star formation histories of a single galaxy in our sample. The EW grids and spatially resolved plots are color coded according to likely stellar classifications (i.e. dark blue represents O-type, pink represents B-type, and yellow represents A-type). *Left:* EW grids Hγ *Middle:* EW grids Hδ *Right:* Spatially resolved galaxies

Parameter	Value	Description
$\log(Z/Z_\odot)$	-1.06	Stellar Metallicity of the composite SFH model
$\log(Z/Z_\odot)$	-1.06	Gas-Phase Metallicity of the composite SFH model
$\log(M/M_\odot)$	6.63	Total Stellar Mass of the composite SFH model
$\log(SFR/M_\odot)$	-1.16	SFR of the recent burst in the composite SFH model
t	10^6	Timescale of the recent burst in the composite SFH model
log(U)	-1.75	Effective Galaxy-Wide Ionization Parameter
ϵ	0.1	Effective Galaxy-Wide Dust-to-Metal Mass Ratio
μ	0.3	Fraction of Attenuation Optical Depth from the Diffuse ISM

TABLE IV. Constraints in metallicity, stellar mass, sSFR, timescale of a recent burst, ionization parameter, dust-to-metal mass ratio, and attenuation. The metallicity, stellar mass, and sSFR are all specific to galaxy J1418, defined in [6]. The remaining values are more general and are defined in [5]

.

(1) Two contain stellar complexes that fall within the age range of A-type stars
(2) Four contain stellar complexes that fall within the age range of O-type stars
(3) All six contain stellar complexes that fall within the age range of B-type stars
(4) Four contain stellar complexes that fall within two of the three age ranges
(5) One contains stellar complexes within all three age ranges
(6) One contains stellar complexes within one age range

Knowing the age distribution of stellar complexes in a galaxy is critical to learning more about their star formation histories. Upon their eventual core-collapses, older (A-type) stars are responsible for creating galactic winds, and hence "holes" in the interstellar clouds. Meanwhile, as younger (O-type) stars radiate great amounts of energy, they are responsible for creating Lyman continuum photons. Many of the stellar complexes in our galaxy sample fall within the ambiguous region between likely A-type and O-type stellar populations. Therefore, it is unclear whether these stars (within the pink region in Figure 3) are young enough to radiate Lyman continuum photons, old enough to produce galactic winds from their core-collapse supernovae, or neither. As long as this remains unknown, the uncertainties remain, regarding the escape of Lyman continuum photons into the IGM during the EoR.

IV. NEXT STEPS

There are many trends in star formation histories amongst pairs of galaxies; however, there are few consistencies that apply to the entire sample. In the future, we plan to define smaller stellar complexes in each galaxy. This will provide greater insight on the star formation histories in these EoR local analogs. Smaller stellar complexes will provide a more detailed map of star formation histories in these galaxies. Through comparing these intricate maps to the general ones presented in this paper, we can better understand how galaxies, specifically EoR local analogs, formed and evolve.

Additionally, in the future, we plan to more thoroughly study some of the galaxies in our sample. Galaxy J0944 has a very interesting morphology and star formation history. Further studying this galaxy's general kinematics and metal content can provide great insight on –. Galaxy J1016 has much higher spatial resolution, as it is closer to us that most of the galaxies in our sample. With this said, more stellar complexes can be identified and analyzed. Additionally, according to the more general map of star formation history in J1016, there are A-type, B-type, and O-type stars present. This presence of A-type and O-type stars supports the theory that Lyman continuum photons escape into the IGM via "holes" in the ISM, created from core-collapse supernovae. To further understand what this theory would entail, we can more thoroughly analyze J1016.

ACKNOWLEDGMENTS

I would like to thank my team for their guidance and support during my time working on this project. I am forever grateful for Professor Crystal Martin and Zixuan Peng, as they made great efforts to help maximize my learning experience. I would also like to thank Yuan Li for assisting me in installing and working stellar population synthesis (SPS) model `BEAGLE`. Our weekly team lunches were very insightful, enjoyable, and memorable. Additionally, I would like to acknowledge UCSB REU site director, Dr. Sathya Guruswamy, for seamlessly organizing this summer's physics REU program. The countless presentations and workshops taught me invaluable skills that I will carry through my professional career. I would also like to thank my family for their support during this

milestone in my academic career. Lastly, I gratefully acknowledge the National Science Foundation for sponsoring and facilitating this research project. This work was supported by NSF grant PHY-1852574.

[1] B. E. Robertson, R. S. Ellis, J. S. Dunlop, R. J. McLure, and D. P. Stark, Early star-forming galaxies and the reionization of the universe, Nature **468**, 49 (2010).
[2] D. A. Berg, B. L. James, T. King, M. McDonald, Z. Chen, J. Chisholm, T. Heckman, C. L. Martin, D. P. Stark, A. Aloisi, R. O. Amorí n, K. Z. Arellano-Córdova, M. Bayliss, R. Bordoloi, J. Brinchmann, S. Charlot, J. Chevallard, I. Clark, D. K. Erb, A. Feltre, M. Gronke, M. Hayes, A. Henry, S. Hernandez, A. Jaskot, T. Jones, L. J. Kewley, N. Kumari, C. Leitherer, M. Llerena, M. Maseda, M. Mingozzi, T. Nanayakkara, M. Ouchi, A. Plat, R. W. Pogge, S. Ravindranath, J. R. Rigby, R. Sanders, C. Scarlata, P. Senchyna, E. D. Skillman, C. C. Steidel, A. L. Strom, Y. Sugahara, S. M. Wilkins, A. Wofford, and X. Xu, The COS legacy archive spectroscopy survey (CLASSY) treasury atlas, The Astrophysical Journal Supplement Series **261**, 31 (2022).
[3] J. Chevallard and S. Charlot, Modelling and interpreting spectral energy distributions of galaxies with beagle, Monthly Notices of the Royal Astronomical Society **462**, 1415 (2016).
[4] P. Morrissey, M. Matuszewski, D. C. Martin, J. D. Neill, H. Epps, J. Fucik, B. Weber, B. Darvish, S. Adkins, S. Allen, R. Bartos, J. Belicki, J. Cabak, S. Callahan, D. Cowley, M. Crabill, W. Deich, A. Delecroix, G. Doppman, D. Hilyard, E. James, S. Kaye, M. Kokorowski, S. Kwok, K. Lanclos, S. Milner, A. Moore, D. O'Sullivan, P. Parihar, S. Park, A. Phillips, L. Rizzi, C. Rockosi, H. Rodriguez, Y. Salaun, K. Seaman, D. Sheikh, J. Weiss, and R. Zarzaca, The keck cosmic web imager integral field spectrograph, The Astrophysical Journal **864**, 93 (2018).
[5] Z. Peng, C. L. Martin, P. Thibodeaux, J. Zhang, W. Hu, and Y. Li, Using kcwi to explore the chemical inhomogeneities and evolution of j1044+0353 (2023), arXiv:2308.00351 [astro-ph.GA].
[6] D. A. Berg, J. Chisholm, D. K. Erb, E. D. Skillman, R. W. Pogge, and G. M. Olivier, Characterizing extreme emission-line galaxies. i. a four-zone ionization model for very high-ionization emission, The Astrophysical Journal **922**, 170 (2021).
[7] L. J. Kewley, D. C. Nicholls, and R. S. Sutherland, Understanding galaxy evolution through emission lines, Annual Review of Astronomy and Astrophysics **57**, 511 (2019).
[8] C. Conroy, Modeling the panchromatic spectral energy distributions of galaxies, Annual Review of Astronomy and Astrophysics **51**, 393 (2013).
[9] G. M. Olivier, D. A. Berg, J. Chisholm, D. K. Erb, R. W. Pogge, and E. D. Skillman, Characterizing extreme emission line galaxies. II. a self-consistent model of their ionizing spectrum, The Astrophysical Journal **938**, 16 (2022).
[10] T. M. Heckman and T. A. Thompson, Galactic winds and the role played by massive stars (2019), arXiv:1701.09062 [astro-ph.GA].
[11] K. T. Soto, C. L. Martin, M. K. M. Prescott, and L. Armus, THE EMISSION-LINE SPECTRA OF MAJOR MERGERS: EVIDENCE FOR SHOCKED OUTFLOWS, The Astrophysical Journal **757**, 86 (2012).
[12] W. R. Freeman, B. Siana, M. Kriek, A. E. Shapley, N. Reddy, A. L. Coil, B. Mobasher, A. L. Muratov, M. Azadi, G. Leung, R. Sanders, I. Shivaei, S. H. Price, L. DeGroot, and D. Kereš, The mosdef survey: Broad emission lines at z=1.4-3.8 (2017), arXiv:1710.03230 [astro-ph.GA].

Appendix A: Appendixes

Accessing Data In each JXXX folder, there is a second folder: JXXXXDS9. This contains the files necessary to run the code in the additional folders. To start, there are the matched galaxy images, from HST or DESI (specified), with the filter in the file name. Additionally, there are the polygon regions extracted for each stellar complex. Lastly, for each galaxy there are the KCWI data cubes for flux and variance spectra.

In each JXXXX_ntbk folder, there are two notebooks: JXXXXsegmdeblend and JXXXXSPEC. The first is used to go through the segmentation and deblending process, then establish the Petrosian radius and Petrosian-based radii. While the elliptical apertures derived from these radii must be extracted manually from DS9 (by entering their centers, major and minor axes, and angle), the free-form polygons can be extracted via the provided code. The second notebook is used to extract the KCWI 1D spectra, using the regions extracted in the other notebook. The wavelength array, spectrum, and variance spectrum that is extracted and saved for each stellar complex in each galaxy is then loaded into the multiple line fitting code (not in one of my notebooks– instead in a separate folder: multiple_line_fitting_test).

Within the multiple_line_fitting_test folder, each stellar complex's flux spectrum and variance spectrum, in addition to the respective galaxy's cumulative wavelength grid is located in the example_inputs subfolder. The line fitting program runs from run_line_fitting.py and creates EW tables (see ew_tables), flux tables (see flux_tables), parameter tables (see parameter_tables), and .png plots of the fit Balmer lines (see plots). Should the line fitting code fail to run properly on a given spectrum, adjust the parameters specified in line_fitting_exec.py.

There is one last set of notebooks, titled J1418_SSP, J1418_constant, and eventually J1418_composite. This set of notebooks is in the J1418_ntbk folder. When mapping the star formation histories for the galaxies in our sample, the BEAGLE mock spectra were all generated from galaxy parameters matching those of J1418. It is unclear the impact this has on our results, and so, it is important the mock spectra are eventually generated for parameters matching the remaining 5 galaxies in our sample. The notebooks created for SSP, constant, and composite in those remaining 5 galaxies will eventually be placed in their corresponding folders.

Included are the fitted emission and absorption spectra, specifically the H-delta and H-gamma Balmer lines, for each stellar complex of each galaxy in our sample. The red lines represent the best fit line, upon fitting the emission peaks and absorption troughs cumulatively. The blue and cyan lines represent the double-Gaussian and/or Lorentzian fits that take into account the multiple emission components or Balmer line absorptions present in the spectra. The Balmer line is labelled and the chi-squared value is defined in the upper right corner of each fit spectrum. As efficient as the line fitting was, there were some Balmer line absorption troughs that were not registered by the fitting program, as they were too broad. Additionally, because the H-beta, H-gamma, and H-delta Balmer lines show troughs of varying sizes, the line fitting program often failed to fit all three in accordance with one another. For this reason, we studied the H-gamma and H-delta Balmer lines to ensure our methods were consistent.

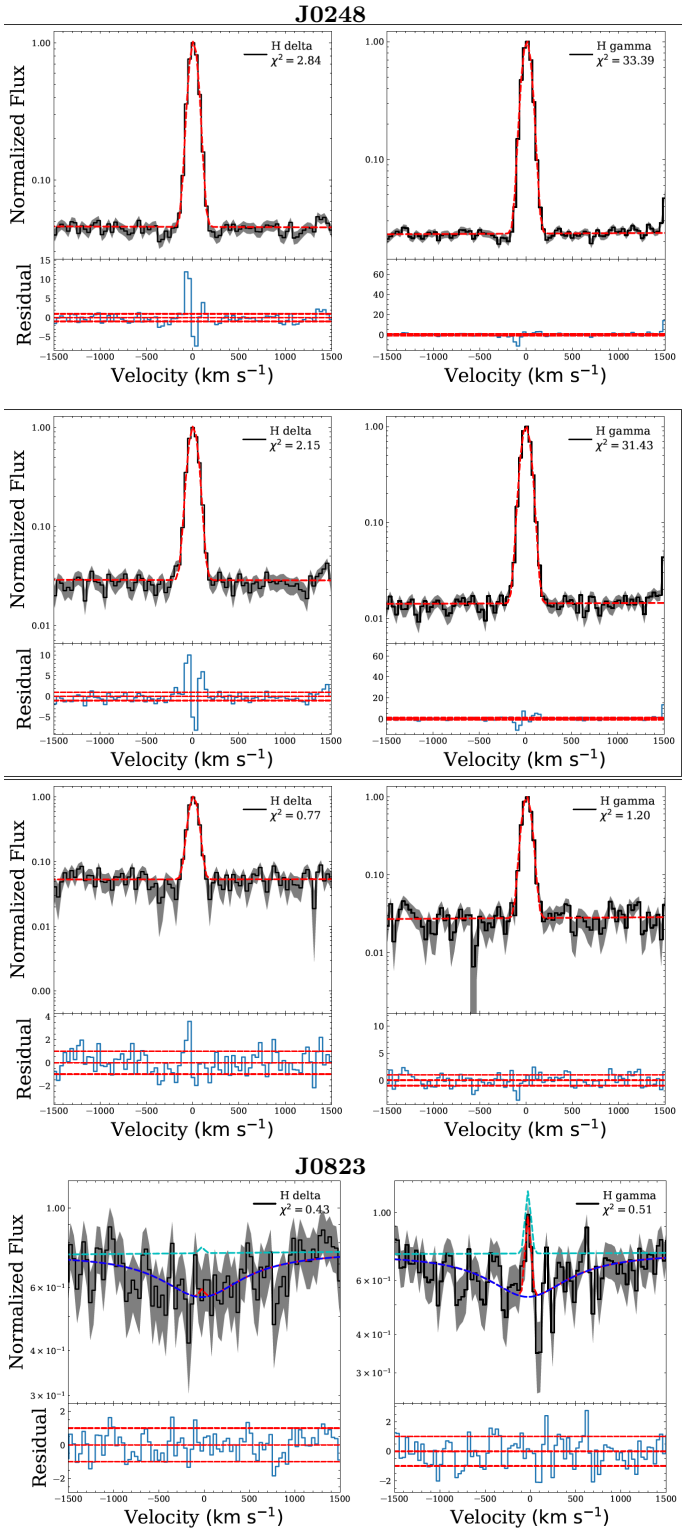
J0248
H delta
$\chi^2 = 2.84$
H gamma
$\chi^2 = 33.39$
H delta
$\chi^2 = 2.15$
H gamma
$\chi^2 = 31.43$
H delta
$\chi^2 = 0.77$
H gamma
$\chi^2 = 1.20$
J0823
H delta
$\chi^2 = 0.43$
H gamma
$\chi^2 = 0.51$
Normalized Flux
Residual
Velocity (km s^{-1})

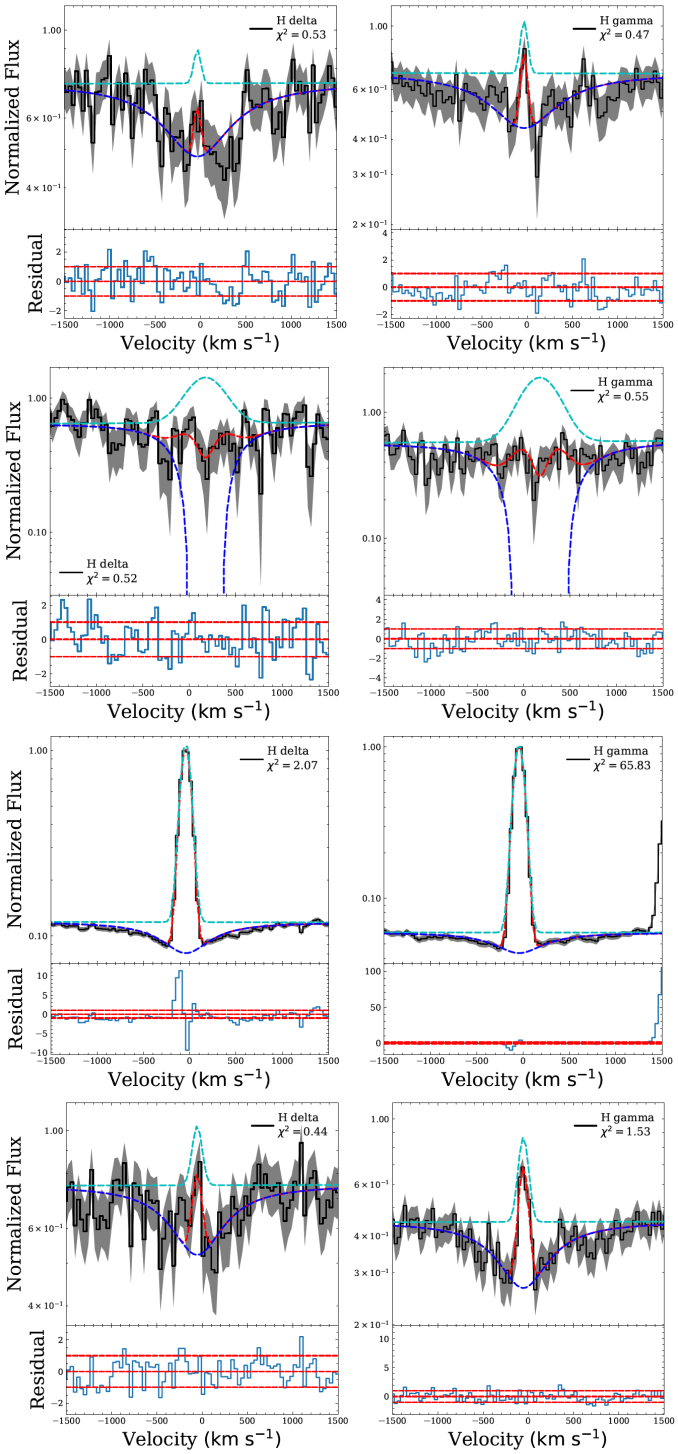
H delta
$\chi^2 = 0.53$
H gamma
$\chi^2 = 0.47$
H delta
$\chi^2 = 0.52$
H gamma
$\chi^2 = 0.55$
H delta
$\chi^2 = 2.07$
H gamma
$\chi^2 = 65.83$
H delta
$\chi^2 = 0.44$
H gamma
$\chi^2 = 1.53$
Normalized Flux
Residual
Velocity (km s^{-1})

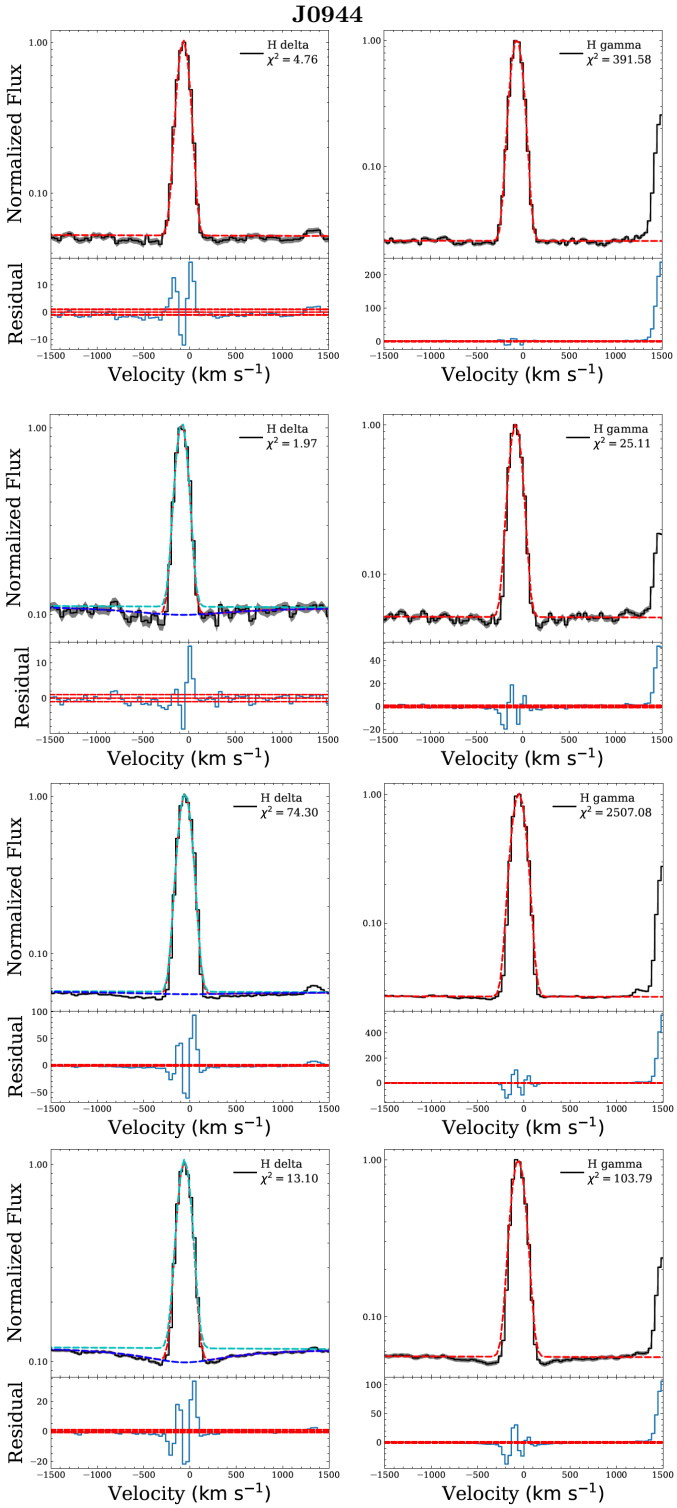
J0944
H delta
$\chi^2 = 4.76$
H gamma
$\chi^2 = 391.58$
H delta
$\chi^2 = 1.97$
H gamma
$\chi^2 = 25.11$
H delta
$\chi^2 = 74.30$
H gamma
$\chi^2 = 2507.08$
H delta
$\chi^2 = 13.10$
H gamma
$\chi^2 = 103.79$
Normalized Flux
Residual
Velocity (km s^{-1})

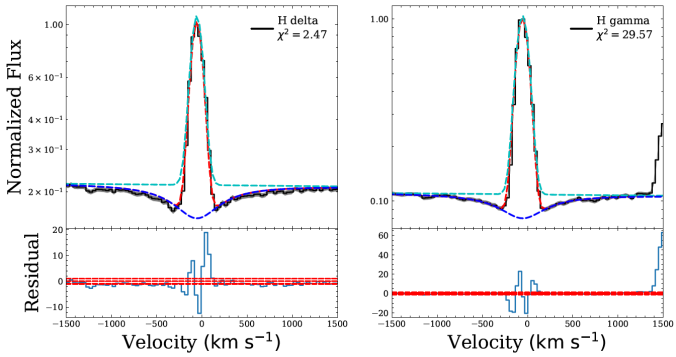
H delta
$\chi^2 = 2.47$
H gamma
$\chi^2 = 29.57$
Normalized Flux
Residual
Velocity (km s^{-1})

J1016

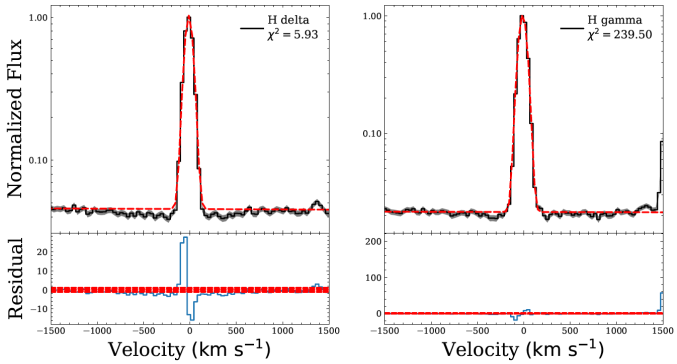
H delta
$\chi^2 = 5.93$
H gamma
$\chi^2 = 239.50$
Normalized Flux
Residual
Velocity (km s^{-1})

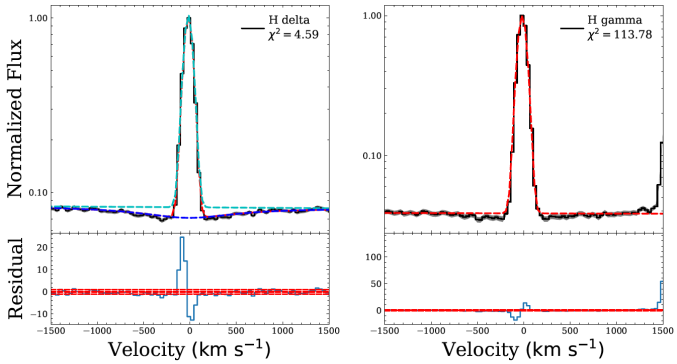
H delta
$\chi^2 = 4.59$
H gamma
$\chi^2 = 113.78$
Normalized Flux
Residual
Velocity (km s^{-1})

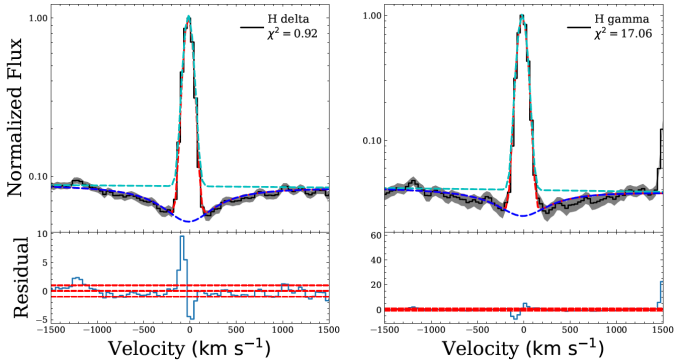
H delta
$\chi^2 = 0.92$
H gamma
$\chi^2 = 17.06$
Normalized Flux
Residual
Velocity (km s^{-1})

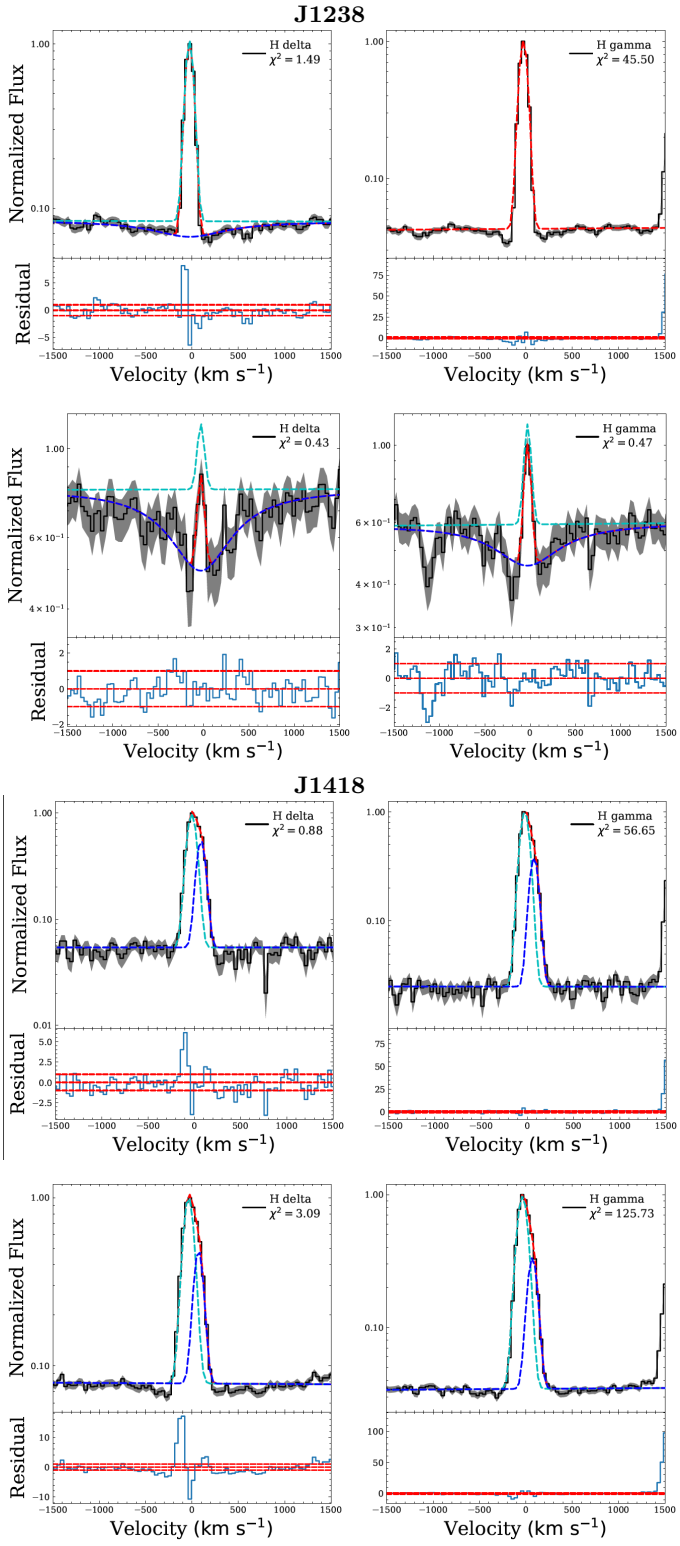
J1238
H delta
$\chi^2 = 1.49$
H gamma
$\chi^2 = 45.50$
H delta
$\chi^2 = 0.43$
H gamma
$\chi^2 = 0.47$
J1418
H delta
$\chi^2 = 0.88$
H gamma
$\chi^2 = 56.65$
H delta
$\chi^2 = 3.09$
H gamma
$\chi^2 = 125.73$
Normalized Flux
Residual
Velocity (km s^{-1})